ScienceAdvances

www.advances.sciencemag.org/cgi/content/full/1/3/e1500109/DC1

Supplementary Materials for

Growth of asteroids, planetary embryos, and Kuiper belt objects by chondrule accretion

Anders Johansen, Mordecai-Mark Mac Low, Pedro Lacerda, Martin Bizzarro

Published 17 April 2015, *Sci. Adv.* **1**, e1500109 (2015)
DOI: 10.1126/sciadv.1500109

This PDF file includes:

Fig. S11. Cumulative size distribution after 3 Myr of coagulation within a population of planetesimals of initial diameters 100 km (50 km in radius), as shown by the cross.
Fig. S12. Formation of planetesimals from centimeter-sized particles in a 2D shearing sheet simulation with the same spatial extent as the streaming instability simulations presented in the main text.
References (*56*–*77*)

Supplementary Materials

A. Johansen, M.-M. Mac Low, P. Lacerda, & M. Bizzarro

1 Materials and Methods

1.1 Sink particles in the Pencil Code

In order to track the masses of the planetesimals as they form and grow, we have developed a new sink particle module for the Pencil Code. Above a threshold particle density value $\rho_{\rm p} = \rho_{\rm p}^{\rm (sink)}$ all particles in the cell are merged to a single sink particle. This sink particle does not feel friction with the gas, due to the large size of the planetesimal. Any particle coming within the distance $\delta x/2$ of a sink particle is destroyed (δx is the size of the resolution element) and its mass and momentum added to the sink particle. In Figure S1 we compare the planetesimal masses arising from simulations at 256^3 with three different values for the sink particle creation threshold. The figure shows that the results are relatively unaffected by the choice of sink particle creation thresholds above 5 times the Roche density. Sink particles allow us to easily keep track of the temporal evolution and saturation of the planetesimal masses, and the merging of several million superparticles into a few sink particles prevents the simulation from slowing down when superparticles cluster on a subset of the available processors (*56*).

1.2 Chondrule accretion simulations

While classical simulations of planetesimal growth focus on the growth by gravitationally focused planetesimal-planetesimal collisions (*20, 21, 57*), the accretion of chondrule-sized objects coupled to the gas via friction can potentially be much more relevant if planetesimals are born and grow in an ocean of chondrules (*23, 24, 58*). "Chondrule accretion" is an aspect of the more general term "pebble accretion", but chondrules are much smaller than the typically cm-sized pebbles used in previous studies of pebble accretion.

1.3 Pebble accretion

Pebble accretion has two dominant regimes. Planetesimals below a transition radius of around 1000 km (at 2.5 AU) accrete pebbles embedded in the sub-Keplerian gas. In the Minimum Mass Solar Nebula (*19*) the relative speed between a planetesimal on a circular orbit and the gas is $\Delta v \approx 50$ m/s. These pebbles are accreted by the planetesimal from the Bondi radius of the planetesimal,

$$R_{\rm B} = GM/(\Delta v)^2\,, \tag{6}$$

provided that the friction time of the pebble matches the time to cross the Bondi radius. Larger pebbles are simply scattered by the planetesimal, while smaller pebbles can not be pulled away quickly enough from the almost straight streamlines of the gas. The finite size of the planetesimal leads to additional complexities, namely gravitational focusing of loosely coupled pebbles; and the Stokes flow of the gas around the planetesimal, which affects the trajectories of strongly coupled particles with impact parameters similar to or smaller than the radius of the planetesimal.

In order to model all these effects correctly we have solved for the trajectories of a large number of pebble-planetesimal combinations, for different values of the friction time $t_{\rm f}$ and the planetesimal radius R. The planetesimal is kept stationary at $(x, y) = (0, 0)$, while the pebble moves under the influence of planetesimal gravity and gas drag. Pebbles enter the simulation domain at a large, positive value of x and with impact parameter $b = y_0$. The gas velocity field is kept fixed and follows the Stokes solution (*59*)

$$u_r = -\Delta v\cos(\theta)\left(1-\frac{3}{2}\frac{R}{r}+\frac{1}{2}\frac{R^3}{r^3}\right)\,, \tag{7}$$

$$u_\theta = +\Delta v\sin(\theta)\left(1-\frac{3}{4}\frac{R}{r}-\frac{1}{4}\frac{R^3}{r^3}\right)\,. \tag{8}$$

Here r and θ are the polar coordinates, with r denoting the distance from the origin and θ the angle between the x-axis and the y-axis, so that the gas flow at large r is uniform along the x-direction $\boldsymbol{u} = -\Delta v\hat{\boldsymbol{x}}$. Collisions with the planetesimal are treated as instantaneous, conserving the total momentum as well as the speed component parallel to the surface and a fraction c of the speed component perpendicular to the surface, with c denoting the coefficient of restitution. The pebble is assumed to be

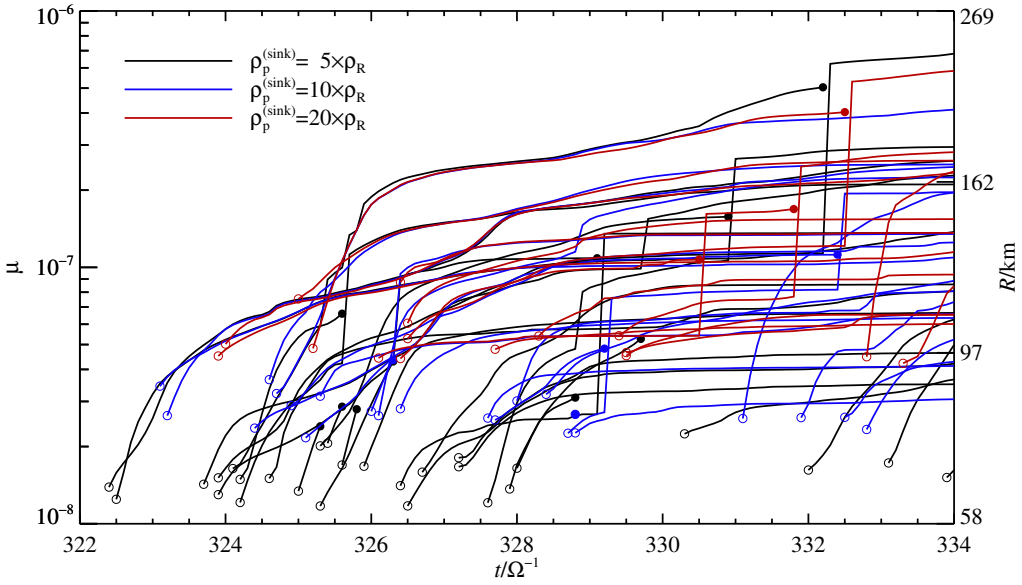

Figure S1: The non-dimensionless planetesimal masses $\mu = \rho_{\rm p}(\delta x)^3$ (here $\rho_{\rm p}$ is the particle density represented by the planetesimal in a grid cell and δx is the size of the cell) and corresponding contracted radii as a function of time after self-gravity is turned on. Simulations at 256^3 grid cells and three different values of the sink particle creation threshold are compared. Creation of a planetesimal is marked with an empty circle, while the destruction is marked with a filled circle. The sizes of the largest planetesimals are relatively unaffected by the choice of the threshold. There are more mergers of small planetesimals at a low sink particle creation threshold, but the planetesimals resulting from those collisions correspond well to the massive planetesimals forming at higher creation thresholds.

accreted after colliding with the planetesimal 5 times or after orbiting the planetesimal 5 times. The latter criterion is convenient for planetesimals with large Bondi radii where the pebble enters a slowly decaying orbit around the planetesimal.

We show the accretion radius $R_{\rm acc}$ (the impact parameter required for accretion) for (a) perfect sticking and (b) a coefficient of restitution of $c = 0.5$ in Figure S2. The accretion radius depends on both the friction time (normalised by the Bondi time $t_{\rm B} = R_{\rm B}/\Delta v$ in Figure S2) and the planetesimal size (normalised by the Bondi radius). We discuss the general trends in the accretion radius curve here:

Large Bondi radius. The gas flow around the planetesimal and the coefficient of restitution play no role in determining the accretion radius when the planetesimal is much smaller than the Bondi radius. This is the case for large planetesimals and/or low relative pebble-planetesimal speeds. The three sections on the growth curve in Fig. S2 are: (i) Strong coupling when the pebble couples to the gas on a much shorter time-scale than the Bondi time-scale. Here the accretion radius is proportional to $R_{\rm B}\sqrt{t_{\rm f}/t_{\rm B}}$. (ii) Weak coupling when the pebble couples to the gas on much longer time-scales than the Bondi time-scale. Here the accretion radius drops rapidly with increasing friction time, with no simple analytical expression. (iii) Gravitational focussing for the largest particles when the weak coupling branch drops below the gravitational focussing radius.

Small Bondi radius. A small planetesimal has Bondi radius much smaller than the planetesimal radius. This limit has two distinct branches: (i) Sedimentation overshoot for strongly coupled pebbles. These pebbles follow the Stokes flow around the planetesimal, but manage to sediment on to the surface for very low impact parameters where the gas flow comes very close to the planetesimal surface. (ii) Geometric accretion for weakly coupled pebbles that do not react to the modified gas flow close to the planetesimals. The latter branch in turn is strongly affected by the coefficient of restitution. Perfect sticking leads to accretion onto the entire projected surface, while consideration of the collision outcome requires very low impact parameters to remain bound after the collision.

Below we discuss some important aspects of the sedimentation overshoot and geometric branches.

Sedimentation overshoot. Small particles are carried with the gas around the planetesimals. The frictional acceleration between gas and particles is nevertheless not instantaneous but operates on the time-scale $t_{\rm f}$. This can lead to accretion of particles that sediment onto the planetesimal surface during the transport around the planetesimal. The gas streamlines at a low impact

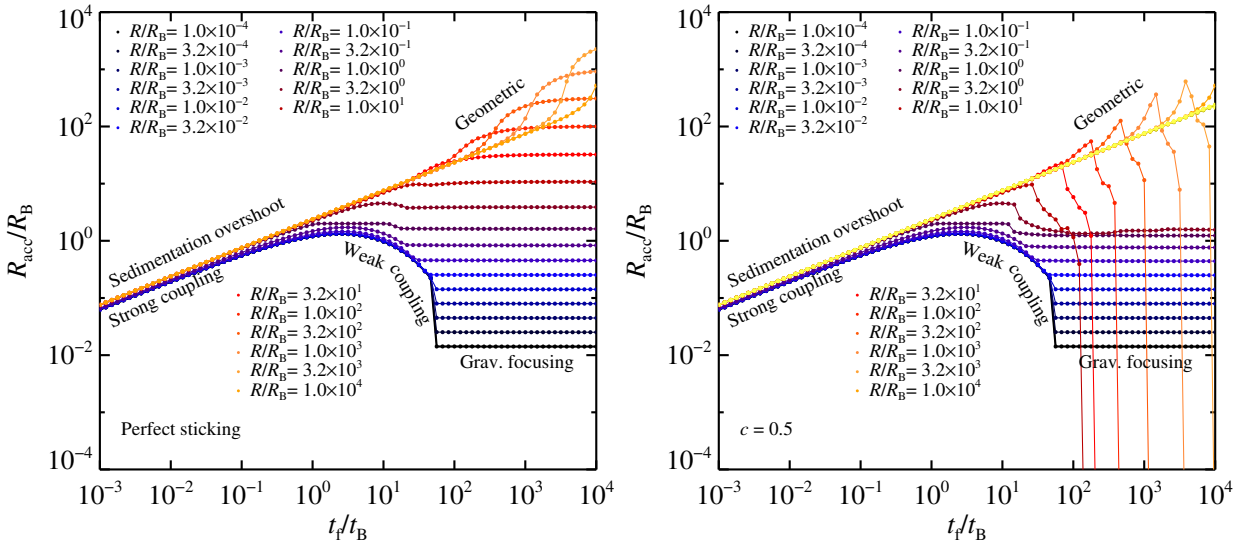

Figure S2: The accretion radius $R_{\rm acc}$ (i.e. the impact parameter required for accretion, given in units of the Bondi radius $R_{\rm B}$) versus the particle friction time $t_{\rm f}$ (in units of the Bondi time-scale $t_{\rm B}$), for planetesimal radii R between $10^{-4}R_{\rm B}$ and $10^{4}R_{\rm B}$. The left panel shows the results when assuming perfect sticking between pebble and planetesimal. Planetesimals with $R < R_{\rm B}$ have three rather distinct branches: strong coupling for short friction times, weak coupling for longer friction times and finally gravitational focusing for the longest friction times. Planetesimals with $R > R_{\rm B}$ radius have two branches: sedimentation overshoot for short friction times (which follows the strong coupling scaling but is physically distinct) and geometric accretion for friction times longer than the time to pass the planetesimal. The consideration of the outcome of the pebble-planetesimal collision, with a coefficient of restitution $c = 0.5$, is shown the right panel. This strongly limits geometric accretion onto small planetesimals.

parameter of $y_0 = b \ll R$ move around the planetesimal at the distance $\delta r \sim b$, at the approximate speed

$$u_\theta \sim \Delta v \frac{b}{R} \,. \tag{9}$$

Ignoring factors of order unity, the time to move around the planetesimal is then

$$\tau_\theta \sim \frac{R}{u_\theta} \sim \frac{R^2}{b\Delta v} \,. \tag{10}$$

During this time the pebble sediments towards the planetesimal at the terminal velocity

$$v_{\rm t} = t_{\rm f} \frac{GM}{R^2} \,. \tag{11}$$

The criterion for reaching the surface is $v_{\rm t}\tau_\theta \sim b$. This in turn yields

$$b^2 \sim t_{\rm f} \frac{GM}{\Delta v} \,. \tag{12}$$

Dividing by the squared Bondi radius finally yields the criterion for accretion

$$\frac{b^2}{R_{\rm B}^2} \sim \frac{t_{\rm f}}{t_{\rm B}} \,. \tag{13}$$

This expression is equivalent to the strong coupling limit of pebble accretion (*24*), although the physics of the accretion via sedimentation overshoot is completely different.

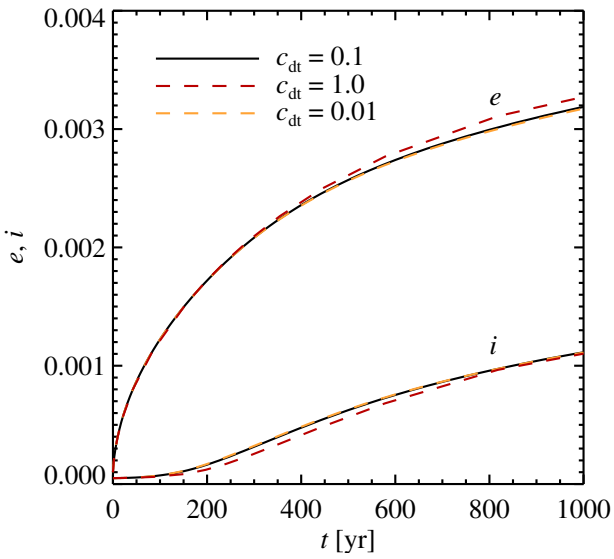

Figure S3: The evolution of eccentricity e and inclination i of 1000 planetesimals with mass $M = 10^{24}$ g located at 1 AU with a surface density of 10 g/cm^2, for three values of the time-step. Here $c_{\rm dt}$ denotes the time-step relative to the collision time-scale. Stirring and dynamical friction are implemented using the scheme described in Ohtsuki et al. (2002). The results are qualitatively similar to Figure 4 of that paper, although the e and i evolve a bit slower in our simulation. We attribute this to a difference in the set up of the simulations: while we initially set $e = 10^{-4}$ and $i = 5 \times 10^{-4}$ for all planetesimals, Ohtsuki et al. (2002) give their planetesimals a Rayleigh distribution around those values. We use $c_{\rm dt} = 0.1$ in the actual planetesimal growth simulations.

Geometric accretion. The requirement that the pebble remains bound after the collision can be found geometrically as

$$R_{\rm acc} = R\sqrt{\frac{(v_{\rm e}/\Delta v)^2 - c^2}{1 - c^2}}\,. \tag{14}$$

Pebbles entering with an impact parameter less than $R_{\rm acc}$ are thus accreted, while pebbles with a larger impact parameter collide once with the planetesimal and then fly off to infinity. The accretion radius is only positive for $c < v_{\rm e}/\Delta v = \sqrt{2}R_{\rm B}/R$. Hence planetesimals with Bondi radii smaller than their size can not accrete pebbles which couple to the gas on time-scales longer than the time-scale to pass the planetesimal (unless c is extremely low).

1.4 Eccentricity and inclination

The growing asteroids experience mutual gravitational encounters that excite the eccentricities and inclinations of the population. This affects the pebble accretion rate since the relative speed between a planetesimal and the sub-Keplerian pebble flow changes with position in the orbit for non-zero eccentricities and inclinations.

The temporal evolution of the eccentricity e and the inclination i is calculated using the analytical approximations of Ohtsuki et al. (*32*), constructed to match the results of N-body simulations for both low and high eccentricities. The analytical evolution equations for e and i give the excitation as well as dynamical friction of a binned population of planetesimals. We show in Figure S3 the result of a test problem defined in Ohtsuki et al. Here we consider 1000 equal-mass planetesimals with initial eccentricity of 10^{-4} and inclination of 5×10^{-5}. The evolution of e and i follows the general curve in Figure 4 of Ohtsuki et al., but the evolution is a bit slower. We attribute this to a difference in the tests. In Ohtsuki et al. the planetesimals are given a Rayleigh distribution of e and i initially, while we assign a constant value equal to the mean of that Rayleigh distribution. A similar test problem with 800 planetesimals is shown in Figure S4, with good agreement with Figure 2 of Stewart & Ida (*60*).

In principle we could use all the planetesimal particles in the code as natural bins and evolve each planetesimal with the dynamical excitation contribution from all other planetesimals. However, this would take unfeasibly long time to compute when there are millions of planetesimal particles. Instead we bin the planetesimals by their radius and consider the dynamical evolution of the smallest and largest planetesimal in each bin. Gravitational stirring is only considered between these anchor planetesimals. The resulting values of $\mathrm{d}e^2/\mathrm{d}t$ and $\mathrm{d}i^2/\mathrm{d}t$ are then multiplied by the total number of planetesimals in the stirring bin, divided

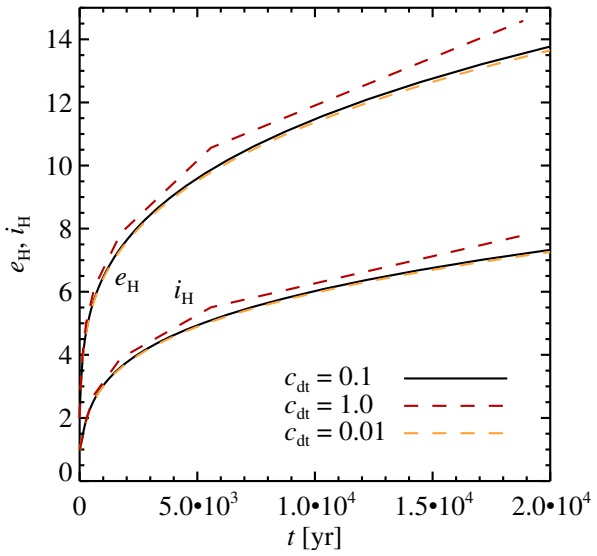

Figure S4: The evolution of eccentricity e and inclination i of 800 planetesimals with mass $M = 10^{24}$ g located at 1 AU with a surface density of 10 g/cm^2. The eccentricity and the inclination are normalised by their Hill values $[2M_{\rm p}/(3M_\star)]^{1/3}$. Results are qualitatively similar to Figure 2 of Stewart & Ida (2000). As in Figure S3, a time-step parameter of $c_{\rm dt} = 0.1$ provides a good compromise between precision and speed; hence we use $c_{\rm dt} = 0.1$ for planetesimal stirring in the planetesimal growth simulations.

by the number of planetesimals that were actually considered (the two anchors). The evolution of e and i is finally interpolated from the anchor planetesimals to all the other planetesimals at the end of the time-step.

The eccentricity and inclination of the orbit can now be used to calculate the pebble accretion rate over a full orbit of the planetesimal. For small eccentricities and inclinations the orbit can be considered in the local coordinate frame corotating with the Keplerian flow at a given distance r_0 from the star. The coordinate system is oriented such that the x-axis points radially away from the star, the y-axis along the orbital direction of the gas and the z-axis perpendicular to the plane of the disk, along the rotation vector of the disk. The epicyclic motion of a planetesimal with eccentricity e in such a frame is

$$v_x(t) = v_{\rm e}\cos(\Omega t)\,, \tag{15}$$

$$v_y(t) = -\frac{1}{2}v_{\rm e}\sin(\Omega t)\,, \tag{16}$$

$$v_z(t) = v_{\rm i}\cos(\Omega t)\,. \tag{17}$$

Here $v_{\rm e} = ev_{\rm K,0}$ and $v_{\rm i} = iv_{\rm K,0}$ are the eccentricity and inclination speeds of the orbit, respectively, measured relative to the Keplerian speed at the centre of the frame, and (v_x, v_y) is the velocity is measured relative to the *local* Keplerian motion at the instantaneous position of the planetesimal. Relative to $v_{\rm K,0}$ the azimuthal velocity is

$$\tilde{v}_y(t) = -2v_{\rm e}\sin(\Omega t)\,. \tag{18}$$

The velocity of the incoming chondrules is $v'_y = -\Delta v$ relative to the local Keplerian velocity. Hence the relative speed between planetesimal and chondrules is

$$v_{\rm rel} = \sqrt{[v_{\rm e}\cos(\Omega t)]^2 + [-(1/2)v_{\rm e}\sin(\Omega t) + \Delta v]^2 + [v_{\rm i}\cos(\Omega t)]^2}\,. \tag{19}$$

The relative speed is lowest at aphelion ($\Omega t = \pi/2$) and highest at perihelion ($\Omega t = 3\pi/2$). Since the Bondi radius scales as $R_{\rm B} \propto 1/v_{\rm rel}^2$, the eccentric motion strongly affects the accretion rate. On the strong coupling branch of pebble accretion one can nevertheless show that the eccentric orbit will not affect the mass accretion rate, because in fact the accretion rate is independent of $v_{\rm rel}$,

$$\dot{M}_{\rm SC} \propto \frac{t_{\rm f}}{t_{\rm B}}R_{\rm B}^2 v_{\rm rel} \propto \frac{t_{\rm f}}{GM/v_{\rm rel}^3}\frac{G^2M^2}{v_{\rm rel}^4}v_{\rm rel} \propto GMt_{\rm f}\,. \tag{20}$$

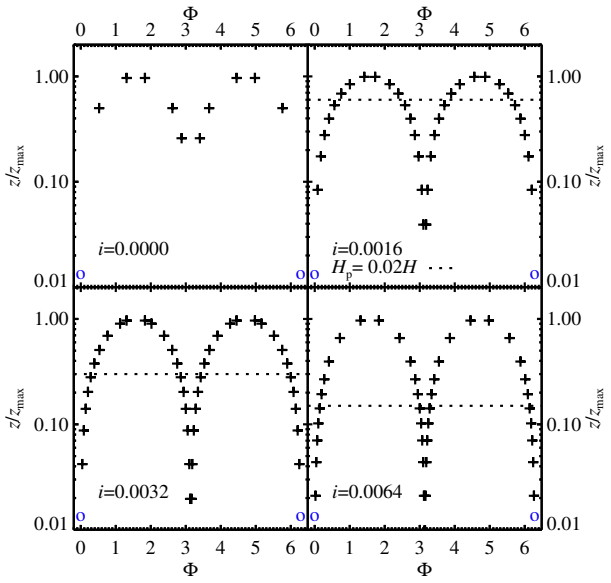

Figure S5: Phase points covering planetesimal orbits with inclinations $i = 0$, $i = 0.0016$, $i = 0.0032$ and $i = 0.0064$. We construct phase arrays to cover both the full planetesimal orbit and the scale-height of the chondrule layer (here $H_{\rm p} = 0.02H$). The height in the planetesimal orbit is normalised by the maximum height for the given inclination. The dotted line indicates the scale-height of the chondrule mid-plane layer, clearly resolved for all choices of the inclination.

At aphelion the relative speed between chondrule and planetesimal can even approach zero for $(1/2)v_{\rm e} \sim \Delta v$. At this point the Bondi radius is no longer the relevant accretion radius as the Hill speed of the planetesimal is higher than the relative chondrule-planetesimal speed, and the planetesimal thus enters short periods of Hill accretion at aphelion (our implementation of Hill accretion is explained in section 1.6).

We take into account the eccentric and inclined orbit of the planetesimal by sampling the accretion rate at a number of phases in the orbit. The choice of phase points is a balance between the need to sample both the scale height $H_{\rm p}$ of the chondrule layer, where chondrule densities are highest, as well as the planetesimal orbit over which the relative planetesimal-chondrule speed, and hence the accretion radius, varies. We set the first phase point at $\Phi = \Omega t = 0$. The distance to the next phase point is taken as the minimum of the two functions

$$\Delta\Phi_1 = \frac{\exp(z/H_{\rm c})H_{\rm c}}{z_{\rm orb}}\frac{2\pi}{N_1}\,, \tag{21}$$

$$\Delta\Phi_2 = \frac{2\pi}{N_2}\,. \tag{22}$$

Here $z_{\rm orb}$ is the maximal height of the planetesimal relative to the mid-plane. This gives phases that cover the full planetesimal orbit, with additional resolution elements added within the chondrule scale height. This way we avoid having to use a very large number of points for highly inclined orbits. We show examples of phase arrays in Figure S5 for $N_1 = 48$ and $N_2 = 12$.

In Figure S6 we show the mass accretion rate of planetesimals at 2.5 AU as a function of the eccentricity of the orbit. We use the approximation that $i = e/2$ and measure the accretion rate relative to that at $e = i = 0$. Increasing the eccentricity actually increases the geometric accretion rate on small planetesimals (below 50 km in radius), since the relative planetesimal-chondrule speed increases and hence the mass flux increases proportionally to the speed. Larger planetesimals are affected negatively by eccentricity. These planetesimals accrete small chondrules at very high rate on circular orbits. The accretion rate at the aphelion of an eccentric orbit does not benefit strongly from the decreased relative planetesimal-chondrule speed at that phase, since the larger Bondi radius requires very large chondrules, which are not present in the disk. Instead the planetesimal enters the strong coupling branch at aphelion, while the accretion rate is strongly reduced at perihelion. The overall result is a reduction in the accretion rate. Even larger planetesimals are affected less and less by the increase in eccentricity. These large planetesimals already accrete on the strong coupling branch, which is relatively unaffected by the relative speed and hence by the eccentricity.

Figure S7 illustrates the mass accretion rates of planetesimals at 25 AU for different values of their eccentricity. The normalised accretion rates in Figure S7 are flat or increasing beyond 200 km in radius, indicating a very steep increase in the accretion rate

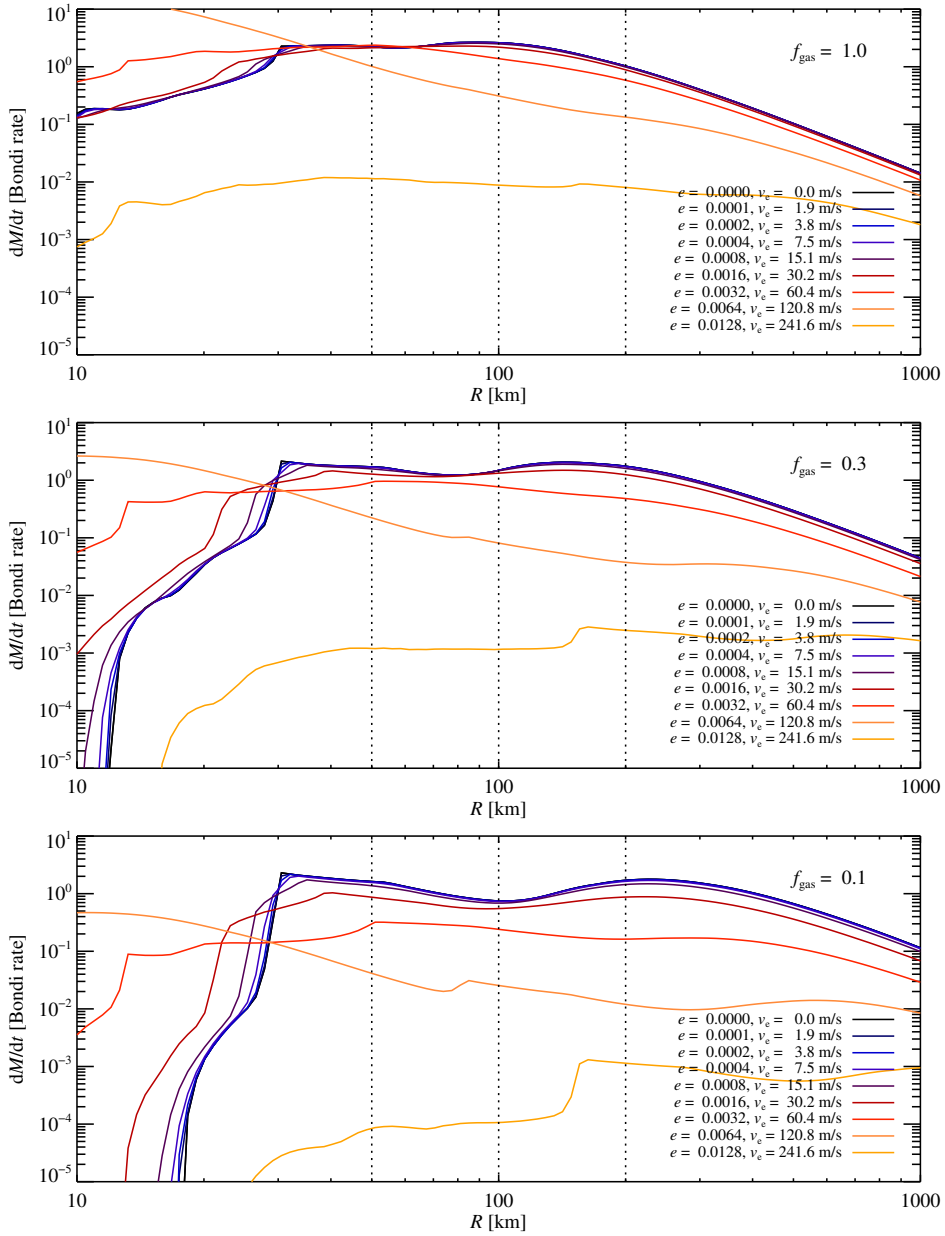

Figure S6: The effect of eccentricity and inclination on the chondrule accretion rate, at an orbital distance of 2.5 AU. The x-axis shows the planetesimal sizes and the y-axis the pebble accretion rate normalised to the accretion rate from the full Bondi radius. Dotted lines mark 50 km, 100 km and 200 km. We use here the approximation $i = e/2$. Increasing the orbital eccentricity can actually increase the accretion rate on bodies smaller than 100 km in radius, as the orbital speed in aphelion matches the sub-Keplerian speed of the chondrules which leads to very high accretion rates. Larger planetesimals are affected negatively beyond the threshold $(e/2)v_{\rm K} = \Delta v$ as the large particles necessary for efficient accretion at aphelion are not present in the disk. The top plot shows results for the column density of the Minimum Mass Solar Nebula at 2.5 AU, the middle plot 0.3 times the MMSN and the bottom plot 0.1 times the MMSN.

with size. This is in contrast to the situation in the asteroid belt where the run-away accretion of chondrules is stopped by the lack of chondrules larger than mm in size (Figure S6).

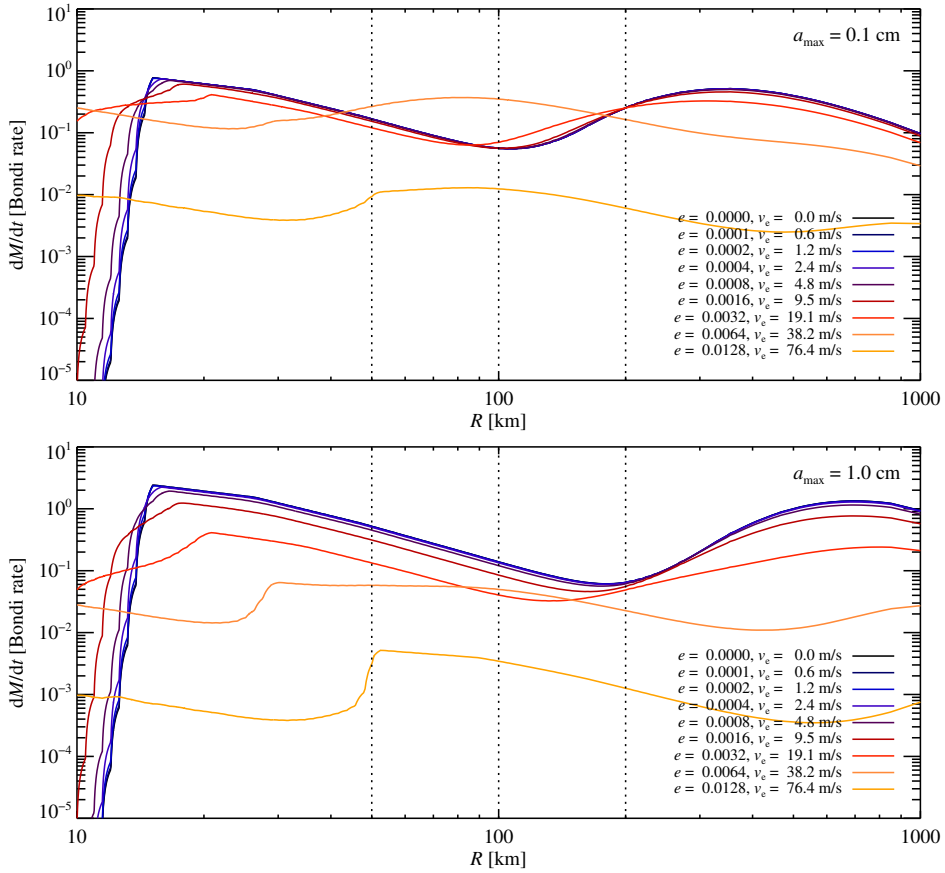

Figure S7: The accretion rate of planetesimals at 25 AU, as a function of the planetesimal size. The accretion rate is normalised by the Bondi rate. The top panel shows the accretion rate for pebbles up to 1 mm in radius, while the bottom panels shows the accretion rate for pebbles up to 1 cm in radius. The accretion rate beyond 200 km in radius is flat or increasing here in the outer regions of the protoplanetary disk. This is in contrast to the situation in the asteroid belt where the lack of chondrules of larger than mm size slows down the run-away accretion of large planetesimals (Figure S6). The presence of mm-cm pebbles in the outer protoplanetary disk can drive a run-away accretion where the most massive planetesimals detach from the rest of the population (see Figure 10).

1.5 Stratification integral

Calculation of the mass accretion rate requires knowledge of the accretion radius as well as the chondrule density averaged over the accretion radius. The stratification integral S is defined as the mean chondrule density normalised by the chondrule density in the mid-plane. The stratification integral for a planetesimal with accretion radius $R_{\rm acc}$ located at the height z_0 over the mid-plane is

$$S = \frac{1}{\pi R_{\rm acc}^2} \int_{z_0-R_{\rm acc}}^{z_0+R_{\rm acc}} \exp[-z^2/(2H_{\rm p}^2)] 2\sqrt{R_{\rm acc}^2 - (z-z_0)^2} {\rm d}z \, . \tag{23}$$

This expression is obtained by summing over lines of constant z and hence constant chondrule density. There is no simple analytical solution to equation (23). Tabularisation of the numerical solution requires interpolation in both $R_{\rm acc}$, z_0 and the angle of incidence of the chondrule flow θ (see below). We therefore an approximation that allows the integral to be calculated analytically. This *square* approximation integrates the chondrule density over a square instead of a circle. This yields the solvable integral

$$S_{\rm square} = \frac{1}{4R_{\rm acc}^2} \int_{z_0-R_{\rm acc}}^{z_0+R_{\rm acc}} \exp[-z^2/(2H_{\rm p}^2)] 2R_{\rm acc} {\rm d}z \, . \tag{24}$$

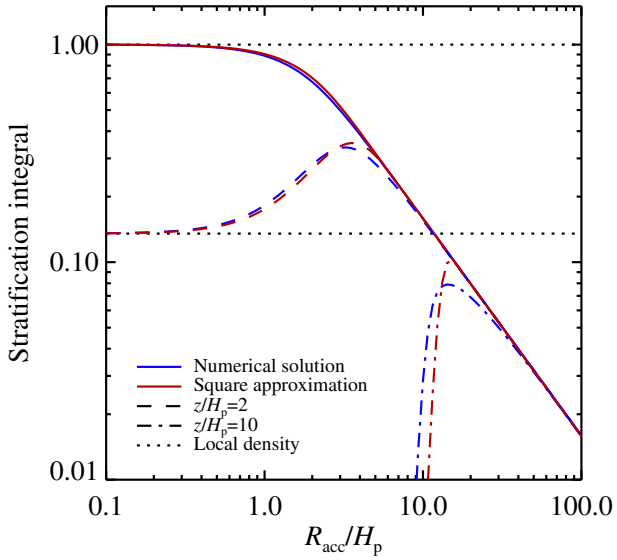

Figure S8: The stratification integral (i.e., the mean particle density over the accretion cross section) as a function of the accretion radius of the planetesimal. Numerical integration of the Gaussian stratification over a circle (blue lines) is expensive, so we use instead a square approximation to the integral (red lines). Full lines indicate a planetesimal in the mid-plane, dashed lines a planetesimal at two times the chondrule scale-height above the mid-plane, and dash-dotted lines a planetesimal at ten times the chondrule scale-height. The square approximation is very precise both when the accretion radius is much lower or much higher than the chondrule scale-height.

The analytical solution is

$$S_{\rm square} = \frac{H_{\rm p}}{\sqrt{2}R_{\rm acc}} \frac{\sqrt{\pi}}{2} \left[{\rm erf}\left(\frac{z_0 + R_{\rm acc}}{\sqrt{2}H_{\rm p}} \right) - {\rm erf}\left(\frac{z_0 - R_{\rm acc}}{\sqrt{2}H_{\rm p}} \right) \right] . \tag{25}$$

The square approximation tends to underestimate the chondrule density because of the inclusion of low-density corners in the square. Therefore we decrease the size of the square by replacing $R_{\rm acc}$ in equation (25) with $R'_{\rm acc} = f R_{\rm acc}$. We have found $f = 0.79$ to give a much better fit to the numerical integral than $f = 1$. In Figure S8 we show how the square approximation compares to the full numerical integration of the accretion radius over the Gaussian stratification.

Planetesimals at very high inclinations encounter the chondrule flow at an angle θ which is $\neq 0°$, measured relative to the vertical. The angle of incidence is found through

$$\theta = {\rm acos}\left(\frac{v_z^{\rm (rel)}}{v_{\rm rel}} \right) \tag{26}$$

Here $v_{\rm rel} = |\boldsymbol{v}_{\rm rel}| = |\boldsymbol{v}_{\rm p} - \boldsymbol{v}_{\rm c}|$ is the vectorial relative speed between the planetesimal (with velocity $\boldsymbol{v}_{\rm p}$) and the chondrules (with velocity $\boldsymbol{v}_{\rm c} = -\Delta v \hat{\boldsymbol{y}}$). The components of $\boldsymbol{v}_{\rm p}$ are given in equations (15)-(17). The consideration of the angle of incidence changes the stratification integral to

$$S = \frac{1}{\pi R_{\rm acc}^2} \int_{z_0 - R_{\rm acc}\cos\theta}^{z_0 + R_{\rm acc}\cos\theta} \exp[-z^2/(2H_{\rm p}^2)] 2 \sqrt{R_{\rm acc}^2 - \left(\frac{z - z_0}{\cos\theta} \right)^2} \frac{{\rm d}z}{\cos\theta} . \tag{27}$$

The square approximation changes to

$$S_{\rm square} = \frac{H_{\rm p}}{\sqrt{2}R_{\rm acc}} \frac{\sqrt{\pi}}{2} \frac{1}{\cos\theta} \left[{\rm erf}\left(\frac{z_0 + R_{\rm acc}\cos\theta}{\sqrt{2}H_{\rm p}} \right) - {\rm erf}\left(\frac{z_0 - R_{\rm acc}\cos\theta}{\sqrt{2}H_{\rm p}} \right) \right] . \tag{28}$$

The results presented in this paper are obtained with the square approximation including the correction for the encounter angle.

1.6 Transition to Hill accretion

Bondi accretion is only valid for planetesimals below a transition mass of approximately 0.1% of an Earth mass (*24*). Beyond this the Hill radius of the growing planetesimal, $R_{\rm H}$, is so large that the relative speed between chondrule and planetesimal is set by the Hill speed $v_{\rm H} = \Omega R_{\rm H}$ rather than the sub-Keplerian speed Δv.

We obtain a smooth transition from Bondi accretion to Hill accretion by solving for the combined speed $v(R_{\rm acc}) = \Delta v + \Omega R_{\rm acc}$. The accretion radius $R_{\rm acc}$ depends on the approach speed, so we solve the equation iteratively from the starting point $v = \Delta v$. This allows us to also apply the tabulated accretion radius for Bondi accretion (Figure S2) to Hill accretion, by modifying the approach speed to take into account the Keplerian shear. We have checked that the resulting accretion rates on the Hill branch are very similar to the results from hydrodynamical simulations (*24*).

1.7 Eccentricity damping by gas drag and chondrule accretion

The planetesimals in our model are so large that the quadratic drag force regime applies, with drag force proportional to the relative speed squared and with friction time

$$t_{\rm f} = \frac{6 R \rho_\bullet}{\delta v \rho_{\rm g}} \,. \tag{29}$$

The drag force can be applied directly to the eccentricity and inclination, following Wetherill & Stewart (1989) (*61*) and Morbidelli et al. (2009) (*21*),

$$\frac{{\rm d}e^2}{{\rm d}t} = -\frac{16}{5}\frac{v}{v_{\rm K}^2}\frac{0.5\pi\rho_{\rm g} v_{\rm g}^2 R^2}{2M(1+0.8\beta^2)} \,, \tag{30}$$

$$\frac{{\rm d}i^2}{{\rm d}t} = -3.2\beta^2\frac{v}{v_{\rm K}^2}\frac{0.5\pi\rho_{\rm g} v_{\rm g}^2 R^2}{2M(1+0.8\beta^2)} \,. \tag{31}$$

Here we use the notation of Morbidelli et al. (2009) who define $\beta = i/e$, $v = v_{\rm K}\sqrt{(5/8)e^2 + (1/2)i^2}$ and $v_{\rm g} = \sqrt{v(v+\Delta v)}$. This formulation damps the eccentricity and inclination to zero on the relevant friction time-scale, with the term $v + \Delta v$ in $v_{\rm g}$ corresponding to an orbitally averaged relative speed which would enter equation (29). We have checked the analytical evolution of e and i against an N-body integration of an eccentric orbit circularised by gas drag and found excellent agreement.

Chondrule accretion and scattering are two additional damping mechanisms. The friction time-scale for chondrule accretion with accretion radius $R_{\rm acc}$ is

$$t_{\rm f,cho} = \frac{M}{\pi R_{\rm acc}^2 \rho_{\rm p} \delta v} = \frac{4}{18}\frac{R^2}{R_{\rm acc}^2}\frac{\rho_{\rm g}}{\rho_{\rm c}} t_{\rm f,gas} \,. \tag{32}$$

We use similar expressions to equations (30)-(31) for the damping by chondrule accretion, but with R^2 replaced by $R_{\rm acc}^2$, $\rho_{\rm g}$ replaced by $\rho_{\rm p}$, and multiplied by $18/4$ to take into account that the pre-factor in the friction time of chondrule accretion $(4/3)$ is much lower than for gas drag (6). Damping by bouncing collisions and chondrule scattering is taken into account by using the maximum of the Bondi radius and the physical radius as the gravitational interaction radius when $t_{\rm f} > t_{\rm B}$ and $R_{\rm acc} < R$.

1.8 Planetesimal growth simulations

The dynamical equations describing the temporal evolution of the masses, eccentricities and inclinations of a large number of planetesimals are solved in a numerical code named "Pebble Accretion Onto Planetesimals and Planets" (PAOPAP), which we have developed for the purpose of demonstrating the importance of chondrule accretion for planetesimal growth. Information about the simulations can be also found in the main paper; here we give some additional details.

The planetesimals are treated as individual particles in the code, each represented by a mass, an eccentricity and an inclination. Planetesimal masses are evolved via the accretion of chondrules and mutual planetesimal collisions (see Section 1.9), while the eccentricities and inclinations are changed by both viscous stirring and dynamical friction from the other planetesimals, as well as damping by gas drag and pebble accretion and scattering. We ignore mass erosion of small (< 50 km) planetesimals by large chondrules impacting and bouncing at super-escape speeds.

The code divides the planetesimals into discrete size bins and calculates $\dot{M}$, $\dot{e}$ and $\dot{i}$ for the smallest and largest planetesimal in each bin. The temporal evolution of all other planetesimals is found by interpolation from the two anchors in each bin. This approach allows us to simulate a high number of planetesimals at a relatively low computational cost and to resolve the run-away growth of a small number of large objects. We use 200 logarithmically spaced bins spanning from 10 km to 10,000 km in radius.

The chondrule density has a Gaussian stratification profile, with the scale-height $H_{\rm p}$ in each bin set according to the diffusion-sedimentation equilibrium expression

$$\frac{H_{\rm c}}{H_{\rm g}} = \sqrt{\frac{\alpha}{\Omega t_{\rm f} + \alpha}} \,. \tag{33}$$

Here $H_{\rm g}$ is the gas scale-height, α is the turbulent viscosity (which we assume takes the same value as the turbulent diffusion coefficient), Ω is the Keplerian frequency at the orbital distance to the asteroid belt and $t_{\rm f}$ is the friction time. The latter is given in the Epstein regime by

$$t_{\rm f} = \frac{a \rho_\bullet}{c_{\rm s} \rho_{\rm g}} \,, \tag{34}$$

with a denoting the particle radius, $\rho_\bullet$ the material density, $c_{\rm s}$ the sound speed in the gas (which depends only on the temperature and the mean molecular weight), and $\rho_{\rm g}$ the gas density. We choose a nominal turbulent diffusion coefficient of $\alpha = 10^{-4}$ (we discuss this choice in the main paper). This yields a scale-height of mm-sized particles of approximately 30% of the gas scale-height, with smaller particles having scale-heights increasing as the square root of their size.

We create chondrules continuously on a time-scale of 1.5 Myr to satisfy the cosmochemical evidence that chondrules in individual chondrites have ages from 0 to 3 Myr (*5*). We have performed test simulations where all the chondrules are present from the beginning; this accelerates chondrule accretion but does not affect the overall picture that asteroids, Kuiper belt objects and planetary embryos grow by chondrule accretion. The chondrules are divided into 30 logarithmically spaced bins, with the number density $n(a)$ distributed according to the size distribution $\mathrm{d}n(a)/\mathrm{d}a \propto a^{-3.5}$.

The planetesimals have initial sizes from 10 to 150 km, distributed in a shallow power law with the differential number following $\mathrm{d}N/\mathrm{d}R \propto R^{-2.8}$, but truncated with an exponential term $\exp[-(R/R_{\rm exp})^4]$ at the planetesimal radius $R_{\rm exp}$=100 km. The smallest planetesimals experience very little growth and act mainly to provide dynamical friction, damping the inclinations and eccentricities of the larger asteroids and planetary embryos.

The pebble accretion rates of the planetesimals are found via interpolation in a look-up table that gives the accretion radius for a grid of values of the planetesimal size $R/R_{\rm B}$ (normalised by the Bondi radius) and the chondrule friction time $t_{\rm f}/t_{\rm B}$ (normalised by the Bondi time). The look-up table is based on a high number of integrations of the dynamics of single chondrules passing by a planetesimal with the sub-Keplerian flow.

The temporal integration of the dynamical equations is done via a simple Eulerian scheme, with the time-step determined to make M, e and i change by a maximum of 10%. We experimented with 30% and found significant changes to the results, while 3% gives very similar results.

1.9 Planetesimal collisions

Planetesimal collisions are included in the code via a Monte Carlo method. The planetesimal particles are first sorted in discrete size bins. For each bin we calculate the average inclination and eccentricity of the planetesimals. We then calculate the collision rate matrix for all combinations of bins, r_{ij}. The collision rates are calculated following the scheme described in the online supplement of Morbidelli et al. (2009) (*21*). We refrain from describing the scheme in detail here since it is already well described in Section 1.1 of the online supplement of Morbidelli et al. (2009) (*21*).

From the time-step of the code we can then calculate the probability P_{ij} that a planetesimal from bin i collides with any of the planetesimals in bin j during the time-step. If a random number r is less than P_{ij} then the planetesimals will be collided. We assume perfect sticking between planetesimals and add the mass of the smaller planetesimal to the larger, removing afterwards the smaller planetesimal from the simulation.

We tested the coagulation scheme against an analytical solution to the coagulation equation where the kernel is constant (*62*). This corresponds to setting the collision rate $r_{ij} = K n_j$, where K is a constant and n_j is the number density of planetesimals in bin j. The solution to the constant kernel test is that the number of bodies remaining at time t is

$$f = \frac{n(t)}{n_0} = \frac{1}{1 + K n_0 t/2} \,. \tag{35}$$

The number of remaining bodies versus time is shown in Figure S9, for different values of the time-step. The time-step is set by

$$\mathrm{d}t = c_{\rm dt} t_{\rm coll} \,, \tag{36}$$

where $t_{\rm coll}$ is the collision time-scale and $c_{\rm dt}$ is a constant time-step parameter. There is excellent agreement in Figure S9 between the analytical expression and the results of the coagulation algorithm, for $c_{\rm dt} < 0.5$. Passing this test implies that the Monte Carlo collision detection scheme is implemented correctly.

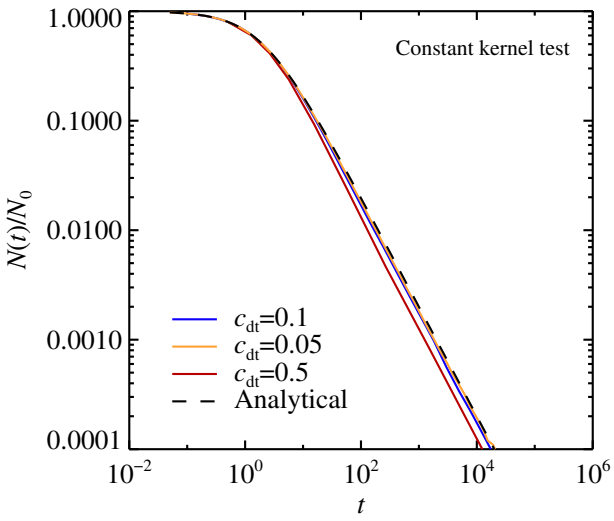

Figure S9: The number of remaining bodies versus time for the constant kernel test. There is an excellent agreement between the results of the coagulation algorithm and the analytical solution for a time-step parameter below $c_{\rm dt} = 0.5$. The time-step parameter is the ratio of the time-step to the collision time-scale.

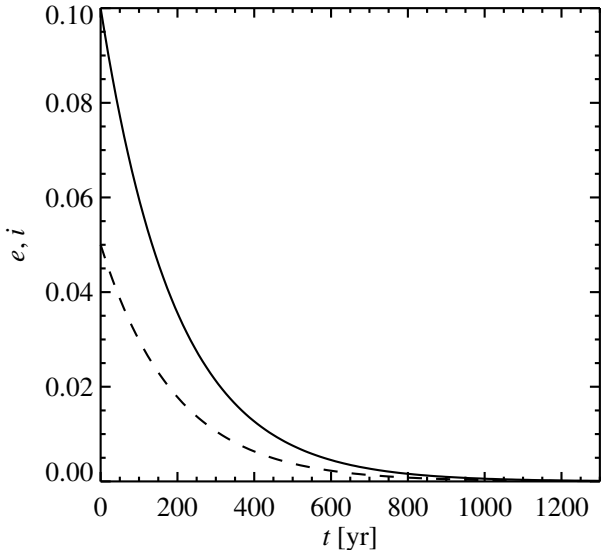

Figure S10: Damping of eccentricities and inclinations of 10,000 1-cm-sized planetesimals located between 30 and 35 AU, emulating a test problem defined in Morbidelli et al. (2009) (*21*). The total mass of the planetesimals is set to 10 Earth masses. The curves agree to within 15% with those shown in Figure 12 of the supplemental material of Morbidelli et al. (2009).

A test of the collision rate calculation can not be done as simply, as the expressions used in Morbidelli et al. (2009) (*21*) are complex. We choose therefore to reproduce one of the figures in that paper, namely a plot of the damping of eccentricities and inclinations of planetesimals due to mutual inelastic collisions. The damping is not very relevant for the large planetesimals considered in this paper, but the exact shape of the damping provides an excellent comparison with the collision rate calculation of Morbidelli et al. (2009) (*21*). The test problem considers 10 Earth masses of 1-cm-sized "planetesimals" located between 30 and 35 AU. Collisions are assumed to be inelastic and lead to energy dissipation; accretion and fragmentation are not included. Figure S10 shows the evolution of the eccentricity (initially 0.1) and the inclination (initially 0.05). There is agreement to within 15% between this plot and supplemental Figure 12 of Morbidelli et al. (2009) (*21*). This shows that the collision rate algorithm

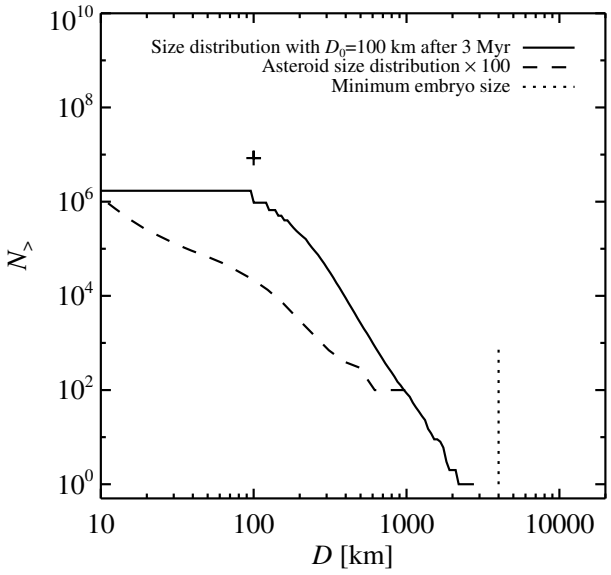

Figure S11: Cumulative size distribution after 3 Myr of coagulation within a population of planetesimals of initial diameters 100 km (50 km in radius), as shown by the cross. The size distribution is much steeper than the current observed size distribution in the asteroid belt. The results presented here are agree to within a few percent with Figure 5 of Morbidelli et al. (2009) (*21*) and Figure 5 of Weidenschilling (2011) (*57*), except for $D > 1000$ km where we have a slight underproduction of embryos. Note that we set the column density of planetesimals equal to that of solids in the Minimum Mass Solar Nebula of Hayashi (1981), while Weidenschilling (2011) uses approximately twice that value.

is likely implemented properly in the PAOPAP code.

An additional test was performed with actual planetesimals. The evolution of a population of 50-km-radius planetesimals was presented in Figure 5 of Morbidelli et al. (2009) (*21*) and Figure 5 of Weidenschilling (2011) (*57*). We performed a similar simulation with our planetesimal accretion code. The resulting cumulative size distribution is shown in Figure S11. The cumulative size distribution is very steep and terminates just before reaching embryo sizes. This steep cumulative size distribution agrees to within a few percent with the results of Morbidelli et al. (2009) (*21*) and Weidenschilling (2011) (*57*), except for a slightly smaller production of the very largest embryos in our simulations. Note that these authors include fragmentation of planetesimals in their calculations, while we ignore this effect. The agreement of the results for $D > 20$ km shows that planetesimal fragmentation plays little role for the coagulation of such large planetesimals. It is well-known that planetesimals larger than 100 km are strong and can survive high collision speeds (*20*).

2 Supplementary Text

2.1 Planetesimal formation in the asteroid belt

The particle sizes used in our streaming instability simulations correspond to approximately 25-cm-sized rocks at 2.5 AU in the Minimum Mass Solar Nebula (Stokes number $\mathrm{St} = 0.3$). This is much larger than the typical diameters of chondrules. We have chosen to study the formation of planetesimals from such large particle sizes in order to have a clean convergence test in parameters employed in previous works (*13, 14*). We suggest three ways to understand the actual formation of planetesimals in the asteroid belt:

1) Chondrule aggregates. Chondrules are covered with rims of fine-grained matrix (*4*) and these rims can facilitate the formation of chondrule aggregates. If the turbulent speed of the gas is very low, with turbulent viscosity $\alpha \sim 10^{-6}$, then collision speeds between rimmed chondrules are low enough to allow chondrules to stick together (*17*). The porous rims act as shock absorbers and facilitate the formation of decimeter-sized chondrule aggregates. These aggregates are large enough to trigger streaming instabilities and the direct formation of planetesimal seeds that can go on to accrete individual chondrules, as envisioned in the main paper. The radial drift speed of these aggregates is high, approximately 10 m/s, causing the aggregates to drift inwards within a few thousand years (*63*). The combination of growth and drift provides a means (a) to form planetesimals from such aggregates and (b) to subsequently flush these aggregates towards the inner solar system, to avoid feeding chondrule aggregates to the largest planetesimals, as this would trigger a very efficient run-away growth of asteroids and give a too steep size distribution.

2) Large chondrules. Another possibility is that the first planetesimal seeds formed out of centimeter-sized macrochondrules (*16*). These could have drifted out of the asteroid belt subsequent to planetesimal formation and left the stage for accretion of their millimeter-sized counterparts. Carrera, Johansen, & Davies (*45*) investigate the ability for the streaming instability to form dense filaments in particles down to chondrule sizes. While chondrule-sized particles are very hard to concentrate, particles just a few times larger (Stokes number of 0.01) concentrate readily into filaments at a particle mass loading of a few times the nominal value in the solar protoplanetary disk ($Z_\odot \sim 0.01$). Here we explore whether these conditions are susceptible to planetesimal formation, by including the self-gravity between centimeter-sized particles (Stokes number of 0.01, so 30 times smaller than in the simulations presented in Figure 3 of the main paper). We use 2-D shearing sheet simulations and set the mean particle density to 1, 3 and 10 times the gas density, respectively, to mimic the mid-plane conditions seen in Carrera, Johansen, & Davies (*45*). The results are shown in Figure S12. The simulations with particle density $\rho_\mathrm{p} = 3\rho_\mathrm{g}$ and $\rho_\mathrm{p} = 10\rho_\mathrm{g}$ form a single planetesimal after a few hundred years. These planetesimals have a characteristic radius of approximately 100 km. This shows that planetesimals can indeed form out of particles as small as 1 cm in size and that the resulting planetesimal sizes are similar to those seen in Figure 3 of the main paper. Thus we show that asteroids can form from centimeter-sized particles. The full exploration of the relevant parameters for formation of planetesimals from centimeter-sized particles is beyond the scope of this paper, but this should have a high priority in future research.

3) Icy pebbles. It is possible that the ice line in the solar protoplanetary disk was much closer to the star in the earliest phases of protoplanetary disk evolution. Hence the asteroid belt could have been populated originally with icy pebbles of sizes comparable to what we used in the simulations (*64*). The first generation of icy asteroid seeds could subsequently have dried out after heating by ^{26}Al or simply have been swamped in the subsequent accretion of dry chondrules. Carbonaceous chondrites display a wide range in their degree of aqueous alteration, consistent with the accretion and subsequent melting of icy pebbles (*3*). However, even some ordinary chondrites have been shown to have experienced water flows (*65*); and hence the formation of the seeds of the nowadays dry ordinary chondrites could have involved accretion of icy material.

Irrespective of the details of asteroid formation, the important factors for our chondrule accretion model are (i) planetesimals form, (ii) the planetesimals are not too small to prevent significant chondrule accretion, and (iii) planetesimals are not so large that all chondrules are accreted on the largest objects in the population. The computer simulations of planetesimal formation by streaming instabilities inspire us to take asteroid seeds with characteristic radii of 100 km and with a fairly shallow size distribution that puts most of the mass in the largest bodies.

2.2 Particle growth and chondrule precursors

In our model we assume that the centimeter-to-decimeter-sized particles discussed in the previous section were only present during the earliest stages of planet formation when the planetesimals formed. Ice particles could only exist while the ice line was interior of the asteroid belt, while the formation of chondrule aggregates requires very weak turbulence of $\alpha \sim 10^{-6}$ (*17*), which may have required an extensive dead zone in a young (and hence still massive) protoplanetary disk. In this section we discuss why the later stages of the protoplanetary disk were likely dominated by chondrule-sized particles.

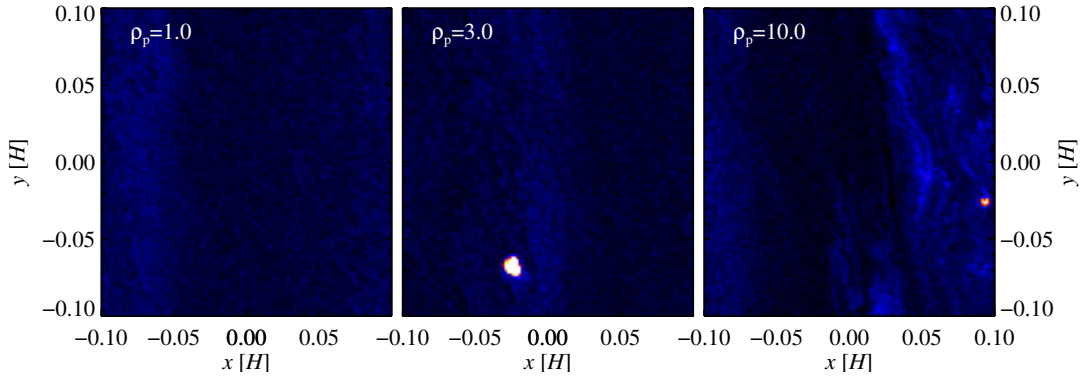

Figure S12: Formation of planetesimals from centimeter-sized particles in a 2-D shearing sheet simulation with the same spatial extent as the streaming instability simulations presented in the main text. The mean particle density is $\rho_{\rm p} = 1$ in the left panel, $\rho_{\rm p} = 3$ in the middle panel and $\rho_{\rm p} = 10$ in the right panel (relative to the gas density). The mean density is set to mimic the effect of both stratification and filament formation by the streaming instability. The simulations with $\rho_{\rm p} = 3$ and $\rho_{\rm p} = 10$ form a single, large planetesimal of approximately 100 km in radius after a few hundred years of integration. This numerical experiment shows that planetesimals can form for particle sizes corresponding to centimeter-sized macrochondrules and that planetesimal sizes are similar to those forming out of 25-cm-sized particles presented in Figure 3 of the main text.

The growth of dust particles in protoplanetary disks happens initially through sticking collisions that lead to the formation of fluffy dust aggregates; see the review paper on coagulation and planetesimal formation by Johansen et al. (*1*). These aggregates are compactified by mutual collisions as they reach approximately millimeter sizes. Compact dust aggregates have poor sticking properties and bounce off each other when they collide (*66*). This *bouncing barrier* is a major obstacle for dust growth (*67*), which could otherwise continue to much larger sizes (*68, 69*). Particles can still grow by mass transfer in high-speed collisions; however the growth rates remain too low to compete against radial drift (*70*). Another possibility is that ice particles could be extremely fluffy and experience perfect sticking even at high speeds (*71*). This nevertheless requires aggregates to consist of very small monomers (0.1 μm), while matrix in chondrites is typically at least 10 times larger.

Hence it appears that the growth of silicate dust grains in the asteroid formation region stops at around mm sizes. This bouncing barrier picture fits well with the sizes of chondrules found in chondrite meteorites. The actual formation process of chondrules is highly uncertain, but is believed to involve heating of dust aggregate precursors in shocks (*72, 73*), in current sheets (*74*) in the protoplanetary disk or in impacts between molten planetesimals (*75*). Our model does not include the presence of chondrule precursors. Such precursors could have a low fractal dimension and hence low friction time, which would prevent sedimentation and efficient incorporation into the asteroids and embryos that grow in the mid-plane. Nevertheless the inclusion of chondrule precursors would not change the conclusions of our paper, as they would simply lead to a slightly higher accretion rate for asteroids and embryos.

2.3 Depletion of the asteroid belt

The current mass of the asteroid belt is only approximately 5×10^{-4} Earth masses. This contrasts with the extrapolation of the Minimum Mass Solar Nebula into the asteroid belt, which yields a particle column density of 4.3 g/cm^2 and hence a primordial mass of 0.86 Earth masses. The depletion of the asteroid belt has happened mainly through collisional grinding and pumping of the eccentricity of asteroids in resonances with Jupiter. Based on a number of arguments, including the extant number of asteroid families and the number of large craters on Vesta, Bottke et al. (*20*) concluded that the collisional activity in the asteroid belt, after excitation of the asteroids to their current eccentricities, can not have been much larger than the current collision rate over 10 Gyr. Hence the asteroid belt must have been depleted to near its current mass very soon after asteroid formation. Morbidelli et al. (*21*) calculate that the asteroid belt could have lost only 1/3 of its current mass over a 10 Gyr equivalent of its present collisional activity. This low level of collisional grinding implies that the current size distribution of asteroids larger than 60 km in radius is primordial (*20*).

The formation of embryos in the asteroid belt provides a means to excite the smaller asteroids to their current, high eccentricities (*25*). Embryos can also be responsible for the rapid clearing of the asteroid belt, since asteroids are gravitationally scattered by the embryos and hence move readily to resonances with Jupiter from which they are removed from the belt (*76*). Hence the

formation of planetary embryos in our chondrule accretion model is completely consistent with mechanisms for depletion of the asteroid belt.

The main alternatives to the embryo model for asteroid belt depletion are (i) sweeping resonances (*26*) and (ii) the migration of Jupiter in the Grand Tack model (*27*). The migration of Jupiter and Saturn during the restructuring of the giant planets to their current orbits by scattering of the primordial Kuiper belt leads to a sweeping of resonant locations across the asteroid belt. This could have led to the loss of 90-95% of the mass of the asteroid belt during the migration period (*26*). The Grand Tack model provides a more violent means for Jupiter's gravity to interfere with the asteroid belt, as Jupiter migrates through the asteroid belt twice; the change from inwards to outwards migration is caused by the formation of Saturn, which comes to share a gap with Jupiter in the protoplanetary disk. This injects C-type asteroids from beyond the ice line into the asteroid belt, which ends up strongly depleted; the later planetesimal-driven migration could inject further icy planetesimals into the main belt (*77*).

Our simulations show that embryos form readily in the asteroid belt from the accretion of chondrules onto planetesimals. These embryos could have played an important role in sculpting the current orbits of the asteroids and depleting the asteroid belt. There are, as discussed above, mechanisms for the depletion of the asteroid belt that do not require the presence of embryos there. The reality could be that a combination of embedded embryos, sweeping resonances and Jupiter's migration conspired to deplete the asteroid belt to its current mass.